Dark Field Differential Dynamic Microscopy enables the accurate characterization of the roto-translational dynamics of bacteria and colloidal clusters

Roberto Cerbino[1], Davide Piotti[1], Marco Buscaglia[1], and Fabio Giavazzi[1]

1 Dipartimento di Biotecnologie Mediche e Medicina Traslazionale, Università degli Studi di Milano, via F.lli Cervi 93, 20090 Segrate, Italy

E-mail: roberto.cerbino@unimi.it, fabio.giavazzi@unimi.it

Abstract. Micro- and nanoscale objects with anisotropic shape are key components of a variety of biological systems and inert complex materials, and represent fundamental building blocks of novel self-assembly strategies. The time scale of their thermal motion is set by their translational and rotational diffusion coefficients, whose measurement may become difficult for relatively large particles with small optical contrast. Here we show that Dark Field Differential Dynamic Microscopy is the ideal tool for probing the roto-translational Brownian motion of shape anisotropic particles. We demonstrate our approach by successful application to aqueous dispersions of non-motile bacteria and of colloidal aggregates of spherical particles.

1. Introduction

Understanding and quantifying Brownian processes is relevant for soft condensed matter scientists as well as for a wider audience that ranges from biologists to economists [1–3]. As far as colloidal particles are of interest, the erratic nature of their Brownian motion is reflected in the well-known fractal appearance of their trajectories as well as in the irregular change of their orientation in time [4, 5]. In the past, rotational Brownian motion has received considerably less attention than its translational counterpart, in part because characterizing the rotational Brownian motion is more challenging. Most of the characterization makes use of optical methods such as Video Particle Tracking (VPT) , Dynamic Light Scattering (DLS), and Fluorescence Correlation Spectroscopy (FCS) [6–9]. In particular, depolarized Dynamic Light Scattering has been shown to be a powerful tool to assess the roto-translational dynamics of an ensemble of anisotropic (by shape and/or optically) particles by analyzing the fluctuations in the depolarized scattered light intensity [6, 7, 10–12]. Very recently, it was shown that depolarized DLS experiments, usually requiring a custom laser-based optical setup, can be performed successfully with an optical microscope [13]. This approach, termed polarized-Differential Dynamic Microscopy (p-DDM), builds on Differential Dynamic Microscopy (DDM) that extracts scattering information from the quantitative analysis of time-lapse microscope movies [14]. While DDM in its original implementation probes the translational diffusion coefficient of a colloidal suspension observed in bright field microscopy, p-DDM gives also access to the rotational diffusion of anisotropic colloidal particles, provided that the sample is observed between suitably oriented polarizers. Compared to DLS and depolarized DLS, DDM and p-DDM offer a simpler implementation, more robust performances, higher flexibility, and a better rejection of both stray and multiply-scattered light [15–17].

Both depolarized DLS and p-DDM work well with spherical particles made of a markedly birefringent material and with non-spherical (optically homogeneous) particles provided that both the shape anisotropy and the optical contrast with the dispersion medium are large enough. These requirements are not always met and, as a result, the rotational dynamics of important classes of particles cannot be probed with depolarized DLS and p-DDM. In particular, particles that are quasi-index matched with the dispersion liquid or sparse aggregates exhibit a depolarized component of the scattered light that is insufficiently large for computing reliably the temporal autocorrelation function of the scattered field (p-DDM) or intensity (depolarized DLS). A quick and reliable tool for the quantitative characterization of the roto-translational dynamics of such samples is not yet available but it would be useful not only for the great potential of anisotropic particles in the self assembly arena [18] but also because many systems of biological interest such as bacteria and prokaryotic cells cannot be easily studied with depolarized DLS [19].

An alternative to depolarized DLS for the characterization of the rotational dynamics of shape anisotropic particles is available, at least for particles that are not too small. In fact, for an anisotropic particle whose longest dimension L is comparable or larger than the inverse scattering wave-vector ($L \gtrsim 150\ nm$, typically), the scattered light intensity depends upon the orientation of the particle itself and from the study of the fluctuations in the scattered light intensity one can measure the so called dynamic form factor [20], which encodes information on the rotational dynamics of the particles, as well as on other internal degrees of freedom, if present [7].

Here we show that Dark Field Differential Dynamic Microscopy (d-DDM), a recently proposed method for the characterization of the translational diffusion of colloidal particles [21], enables also the effective quantification of the intensity fluctuation associated with the rotational dynamics. Our key observation is that, in a conventional dark field microscope, the image of a small particle

is mainly formed by light scattered at relatively large angles, while forward scattered light is not collected. This implies that the intensity associated with the dark field image of an anisotropic particle depends on its orientation. Accordingly, if the particle rotates, for example because of thermal motion, the intensity of the collected light fluctuates, leading to an image that "blinks" over time. This makes d-DDM a valuable tool also for the quantitative characterization of the roto-translational dynamics of colloidal particles, especially in regimes where p-DDM does not work, namely the case of micron-sized particles closely index-matched with the solvent. To demonstrate this approach we first present measurements on a dispersion of non-motile rod-shaped bacteria. The determination of the rotational and translational diffusion coefficients allows to determine the relevant dimensions of the bacterial particles. In a second set of experiments, d-DDM is applied a suspension of spherical colloidal articles containing a small number of aggregates. In this case d-DDM is demonstrated to be extremely sensitive to the presence of the anisotropic aggregates that lead to a significant rotational signal.

2. Materials and methods

2.1. Sample preparation

In order to assess the potential of d-DDM in characterizing the roto-translational dynamics of anisotropic colloidal particles, we have employed two different kind of samples that are difficult to study with other tools such as p-DDM and/or depolarized DLS. In particular, we studied aqueous dispersions of non-motile bacteria and of aggregates of spherical nanoparticles, both presenting shape anisotropy and a moderate refractive index difference with the dispersion medium (water).

Non-motile bacteria One of the most frequently used E. coli strain for routine biological cloning applications is the DH5α strain, which are non flagellated bacteria. They are almost non-motile, less fragile to handle and easy to grow, which makes them the perfect anisotropic particles for our purposes. We grew single colonies from frozen stocks on Luria broth (LB) agar plates at 37 °C overnight. A single colony was transferred from a plate to 20 ml of liquid LB and incubated overnight (16 h) at $37°C$ while shaken (for aeration) at 200 rpm. The next step was to transfer cells from LB to a minimal medium with no exogenous nutrients in order not to have bacterial reproduction and to minimize the growth rate. To this aim, the medium underwent a washing process consisting of a 2 min centrifugation (6000 rpm and 2000 g), the expulsion of supernatant and the resuspension of bacterial pellet in 1 ml of PBS (phosphate-buffered saline, a water-based salt solution containing sodium hydrogen phosphate and sodium chloride). This washing procedure was repeated 3 times (2 centrifugations). After this, the system was sucked into a $0.3 \times 1 \times 20$ mm capillary and the capillary was fixed to a glass slide with vaseline petroleum jelly, a non-toxic glue. This operation was carefully performed in order not to let air get inside the capillary that could lead to unwanted sample drifts. It was also important to carefully avoid liquid residuals between the capillary and the glass slide, which would have caused a dynamic drying front expanding during the microscope acquisition and affecting the DDM experiments.

To avoid bacteria sedimentation, which impact on the dynamics, the density mismatch between bacteria and the PBS physiological medium was compensated by adding Percoll® to the dispersion. Percoll® is routinely used for density gradient centrifugation of cells, viruses, and sub-cellular particles. It consists of colloidal silica particles of $15 - 30$ nm diameter prepared at 23% w/w in water. The silica particles are coated with polyvinylpyrrolidone (PVP), which makes them

completely non-toxic and ideal for use with biological materials. PVP is randomly bound to the silica particles as a monomolecular layer. The size of these particles is so small that the intensity of the scattered light is negligible when compared to the intensity of the light scattered by bacteria, as we checked experimentally in preliminary DDM experiments. We found that a sample made of 20% of PBS medium with bacteria and 80% of Percoll ® was stable upon centrifugation for 2 hours at 2000 g, which is a time longer than the 30-40 minutes needed to acquire microscope videos in bright field and dark field. We note that for large concentrations of bacteria, bacterial aggregation was found to occur in the presence of Percoll ®, an effect presumably due to depletion interactions. For this reason we worked at a low bacterial concentration (about 1×10^5 bacteria/ml, corresponding to a volume fraction of about $\phi = 2 \times 10^{-7}$), below the threshold needed to trigger appreciable aggregation during our experiments. The viscosity of the PBS-Percoll ® solution has been measured by a capillary viscosimeter for temperatures in the range $24-25$ °C. For $T = 24$ °C, the temperature at which the experiments with bacteria have been performed, we found $\eta = (1.87 \pm 0.02)\ 10^{-3}\ Pa{\cdot}s$.

Polystyrene particles We used spherical polystyrene particles (Spherotech (TM) SPHERO (TM) Biotin Polystyrene Particles), with a certified mean diameter equal to 0.74 μm (intensity-weighted Nicomp distribution rescaled to number density). The samples were prepared by gently vortexing the bottle in order to resuspend the colloidal particles. Serial dilutions in 15 mM PBS buffer lead to a final concentration of about 10^5 particles/ml, corresponding to a volume fraction of about $\phi = 2.0 \times 10^{-8}$. The solution was then sonicated for 10 min and confined into a rectangular glass capillary (VITROCOM, internal size: $0.3 \times 1 \times 20$ mm) for the microscopy observations. The capillaries were sealed on both sides with UV glue (UV30-20, Loxeal s.r.l., Cesano Maderno, Italy), cured for 10 min under UV light (VL-6.M, Vilbert Lourmat, Marne la Vallèe, France) and successively loaded on the microscope. The particles concentration was low enough to ensure that single particles could be identified and tracked when observed under the microscope, which allowed a direct-space based characterization of the particles trajectories, in addition to DDM. The viscosity of the PBS solution at the temperature $T = 24$ °C at which the experiments have been performed has been estimated by using literature value for pure water at the same temperature ($\eta = (0.91 \pm 0.01)\ 10^{-3}\ Pa \cdot s$).

2.2. Differential Dynamic Microscopy

Microscopy measurements were performed with a Nikon Eclipse Ti-E commercial microscope equipped with a Hamamatsu Orca Flash 4.0 v2 camera (pixel size $d_{pix} = 6.45$ μm). Dark field images are collected with a $10X$ standard microscopy objective ($(NA)_o = 0.15$), while the sample is illuminated with a condenser stage ($(NA)_s = 0.4$) coupled with a PH3 phase-contrast ring mask. Bright field images are also collected with the same objective lens and bright field illumination, by using the same condenser stage with a standard diaphragm. For bacteria we also used a $40X$ phase-contrast objective ($(NA)_o = 0.6$), the sample being illuminated through the same condenser stage used in the previous cases, using a proper ring mask in order to achieve the phase-contrast condition. Each acquisition typically corresponds to a sequence of $N = 50000$ images $I(\mathbf{x}, t)$ acquired with a frame rate $1/\Delta t_0$ equal to 100 fps in the case of the bacterial suspension and to 20 fps for the latex particles. Movies acquired in dark field microscopy exhibit a characteristic blinking due to the rotation of anisotropic particles, which is not present in bright field or phase contrast movies (see Supplementary Movies SM00 and SM01, respectively). To extract quantitative information from these movies we analyzed them by using the standard DDM algorithm [14, 16, 22], which

is based on calculating the difference $d(\mathbf{x}, t_0, \Delta t) = I(\mathbf{x}, t_0 + \Delta t) - I(\mathbf{x}, t_0)$ between two images acquired at times t_0 and $t_0 + \Delta t$. Once this quantity is obtained, its spatial Fourier power spectrum is computed by using a Fast Fourier Transform (FFT) routine and, in the presence of stationary or quasi-stationary statistical processes, an average over power spectra with the same Δt but different reference time t_0 is obtained, which increases the statistical accuracy of the data. This leads to the so called *image structure function* (ISF)

$$d(\mathbf{q}, \Delta t) = \left\langle \left| FFT[d(\mathbf{x}, t_0, \Delta t)] \right|^2 \right\rangle_{t_0} \tag{1}$$

that captures the dynamics of the sample as a function of the two-dimensional scattering wave-vector $\mathbf{q}$ and of the delay time Δt. The ISF is connected to the (normalized) intermediate scattering function $f(\mathbf{q}, \Delta t)$ [7] by the relation

$$d(\mathbf{q}, \Delta t) = 2A(\mathbf{q}) \left[1 - f(\mathbf{q}, \Delta t)\right] + 2B(\mathbf{q}) \tag{2}$$

where $B(\mathbf{q})$ is a term that accounts for the camera noise, $A(\mathbf{q})$ is an amplitude term that contains information about the static scattering from the sample and details about the imaging system [16]. The form of the intermediate scattering function for a sample observed under dark field imaging, undergoing both translational and rotational Brownian motion will be discussed below in Section 3.1.

In general, the two-dimensional nature of the ISF provides a powerful means to probe the sample dynamics along different directions in the $\mathbf{q}$ plane that may be of particular interest for the problem under study [23]. However, whenever the ISF bears a circular symmetry, as for all the experiment described here, azimuthal averaging of $d(\mathbf{q}, \Delta t)$ is often used to obtain the one-dimensional function $d(q, \Delta t)$, of the radial wave-vector $q = \sqrt{q_x^2 + q_y^2}$ [14, 24–29].

In order to obtain a reliable determination of the sample dynamics, which is encoded in the intermediate scattering function, a robust procedure for estimating the amplitude $A(\mathbf{q})$ and the noise contribution $B(\mathbf{q})$ in Eq. 2 is required. Dark field microscopy experiments are very sensitive to non-idealities such as like dust particles and scratches on the optical elements and/or on the sample cell, which can give a significant background signal on top of which the signal from the particle is superimposed. This background signal appears as an additive, positive term to the image intensity distribution. The intensity distribution $I(\mathbf{x}, t)$ associated with each image can be thus written as the sum of three independent terms:

$$I(\mathbf{x}, t) = I_0(\mathbf{x}) + I_s(\mathbf{x}, t) + I_N(\mathbf{x}, t) \tag{3}$$

where $I_0(\mathbf{x})$ is a background image (*i.e.* the intensity distribution that would be observed in absence of the sample), $I_s(\mathbf{x}, t) \geq 0$ is the contribution to the image from the particles and $I_N(\mathbf{x}, t)$ is the camera noise. In our case, the main contribution to the camera noise is from the shot noise and we can safely assume that it has zero average: $\langle I_N \rangle = 0$ and that it is delta-correlated in both space and time: $\langle I_N(\mathbf{x} + \boldsymbol{\Delta}\mathbf{x}, t + \Delta t) I_N(\mathbf{x}, t) \rangle = \langle I_N^2 \rangle \, \delta(\Delta x) \delta(\Delta t)$. If the amplitude of the noise is small compared with the background intensity $\sqrt{\langle I_N^2 \rangle} \ll \langle I_0 \rangle$ and if the density of the scatterers is low enough to ensure that only a finite fraction of the image is covered by the particles, an accurate reconstruction of the background image can be obtained as $I_0(\mathbf{x}) = \min_t \{I(\mathbf{x}, t)\}$. In fact, by picking up for each pixel the lowest intensity value registered during a suitably large time window - larger than the diffusion time of a single particle over its image - allows to minimize the additive contribution from the particles themselves. Once an estimate for $I_0(\mathbf{x})$ has been obtained, an estimate of the total amplitude of the fluctuating parts can be extracted

from $C(\mathbf{q}) = \left\langle |FFT[I(\mathbf{x},t) - I_0(x)]|^2 \right\rangle = 2A(\mathbf{q}) + 2B(\mathbf{q})$, where we have made use of Eq. 3. Eq. 2 can be thus rewritten in terms of $C(\mathbf{q})$ as

$$d(\mathbf{q},\Delta t) = 2\left[C(\mathbf{q}) - B(\mathbf{q})\right]\left[1 - f(\mathbf{q},\Delta t)\right] + 2B(\mathbf{q}). \tag{4}$$

$B(\mathbf{q})$ can be estimated with high accuracy as the intercept for $\Delta t \to 0$ of $d(\mathbf{q},\Delta t)$. This could be obtained in practice by fitting $d(\mathbf{q},\Delta t)$ over a small interval $[0,\ \Delta t_s]$ to a polynomial function and by taking the 0-th order coefficient. This procedure sets the value $[C(\mathbf{q}) - B(\mathbf{q})]$ of the amplitude of the first term, allowing thus a reliable estimate of the relaxation times in $f(\mathbf{q},\Delta t)$ even if they exceed the width of the acquisition window.

3. Theory

In this Section we will first provide a brief summary of the scattering theory from optically anisotropic particles [7]. In the second part we will describe the features of a dark field imaging system and the imaging process of anisotropic particles.

3.1. Scattering by anisotropic particles

Small anisotropic particles: Rayleigh scattering The description of the scattering of light by a particle much smaller than the wavelength is usually based on the so-called *Rayleigh approximation* [30]. For simplicity, we will restrict our discussion to the case of uniaxial particles, whose polarizability tensor admits a diagonal form with diagonal elements α_1, α_2, α_3, where $\alpha_2 = \alpha_1$. For this kind of particles, the anisotropy parameter is defined as $\beta = \alpha_3 - \alpha_1$ and the average (excess) polarizability as $\alpha = \frac{2\alpha_1+\alpha_3}{3} - V\left(n_s^2 - 1\right)$. Here V is the particle volume and n_s is the refractive index of the dispersion medium. If a plane wave electric field $\mathbf{A_0}(z) = \mathbf{E_0}e^{-jkz}$ of wave-number k impinges on such particle, the latter emits a scattered field that, in addition to the component E_{VV} that is parallel to $\mathbf{E_0}$, also bears a perpendicular component E_{VH}. One has [30]

$$E_{VV} = S_{VV}\frac{e^{-jkr+jkz}}{jkr}A_0(z) \tag{5}$$

and

$$E_{VH} = S_{VH}\frac{e^{-jkr+jkz}}{jkr}A_0(z) \tag{6}$$

where j is the imaginary unit, r is the distance from the particle, and S_{VV} and S_{VH} are dimensionless amplitudes that depend on the scattering angle θ_s measured with respect to the direction z of the incident radiation, and on the orientation (θ,ϕ) of the particle. For small scattering angles, the scattering amplitudes S_{VV} and S_{VH} are given by the following expression [7]

$$S_{VV} = jk^3\alpha + jk^3\beta\sqrt{\frac{16\pi}{45}}Y_{2,0}(\theta,\phi), \tag{7}$$

$$S_{VH} = jk^3\beta\sqrt{\frac{2\pi}{15}}j\left[Y_{2,-1}(\theta,\phi) + Y_{2,1}(\theta,\phi)\right]. \tag{8}$$

Here $Y_{l,m}(\theta,\phi)$ is the spherical harmonic function of order l, m.

Given the shape and the refractive index distribution within a particle, the calculation of its polarizability tensor is not in general a trivial task. Even in the Rayleigh regime, closed-form

expressions can be obtained only in presence of particularly simple geometries. In order to better elucidate how the scattering properties of a particle depend on its shape and refractive index, it can be worth considering a specific model system for which a simple analytical description is available, namely a homogeneous ellipsoid of revolution (spheroid) of semi-axes $[\epsilon R, R, R]$. In this case, the diagonal elements α_j of the (excess) polarizability tensor are given by $\frac{V}{4\pi\alpha_j} = L_j + \frac{1}{m^2-1}$, where $m = n_p/n_s$ is the ratio between the refractive index n_p of the particle and the refractive index $n_s$of the solvent and $L_{2,3} = L$, $L = 1 - 2L$, with $L = \epsilon \int_0^\infty \frac{du}{2(u+1)^2(u+\epsilon^2)^{1/2}}$. L is a parameter ranging from 0 (flat elliptical disk) to $\frac{1}{2}$ (infinitely long ellipsoid). The value $L = \frac{1}{3}$ corresponds to the isotropic case. We can also define an anisotropy factor $a = 2(3L - 1)$ in such a way that $a = 0$ corresponds to a sphere, while one has $a = 1$ for an infinitely long ellipsoid. If we also define $\delta = m^2 - 1$, we obtain the following simple expression for the amplitude depolarization ratio [7]

$$\frac{\beta}{\alpha} = \frac{3\delta a}{6 + \delta\,(2 - a)} \simeq \frac{1}{2}\delta a \tag{9}$$

which in fact is the ratio between the amplitudes of orientation-dependent component and the orientation-independent component of the scattered field in Eqs. 6, 8. It is clear from Eq. 9 that the contrast in the fluctuation of the depolarized scattering component depends both on the anisotropy of the particle and on the refractive index mismatch with respect to the solvent. Even a strongly anisotropic particle ($a \simeq 1$) cannot produce a significant depolarized signal if it is quasi index-matched with the solvent ($\delta \simeq 0$). We note that, as far as the Rayleigh approximation is satisfied, the result expressed by Eq. 9 holds independently of the particle size.

Weakly scattering anisotropic particles of larger size: Rayleigh-Gans-Debye description The case of a homogeneous, quasi-index-matched particle can be adequately described within the *Rayleigh-Gans-Debye (RGD) approximation* if the overall phase delay associated with the particle is small: $|\delta|kd \ll 1$ [30]. In this approximation, the amplitude of the wave scattered by the particle can be calculated as the sum of independent contributions from each portion of particle. In the RGD approximation the amplitude of the depolarized scattering is negligible and the scattering amplitude entails only a polarized component

$$S_{VV}(\mathbf{q}) = \frac{j\delta k^3}{4\pi} V \cdot F(\mathbf{q}) \tag{10}$$

where

$$F(\mathbf{q}) = \frac{1}{V}\int_V d^3x e^{-j\mathbf{q}\cdot\mathbf{x}} \tag{11}$$

is the so-called form factor amplitude and $\mathbf{q} = (\mathbf{k_s} - \mathbf{k_i})$ is the transferred momentum, *i.e.* the difference between the scattering wave-vector $\mathbf{k_s}$ and the wave-vector $\mathbf{k_i}$ of the incident light. For a particle of a given shape, $F(\mathbf{q})$ has in general an implicit dependence on the particle orientation. Within the RGD approximation, the scattering in the forward direction ($\mathbf{q} = \mathbf{0}$) does not depend on the details of the particle shape or orientation, as $F(\mathbf{0}) = 1$. A non-trivial dependence of the scattered amplitude on the particle orientation can be observed only for $q > 0$ and if the size of the particle is not too small compared with the wavelength of light [7].

For a spheroidal particle, such as the one considered in the previous paragraph, the form factor amplitude can be calculated explicitly:

$$F_{ell}(\mathbf{q}) = 3\left[\frac{\sin(qR_\gamma) - qR_\gamma\cos(qR_\gamma)}{(qR_\gamma)^3}\right] \tag{12}$$

where $R_\gamma = R\sqrt{\sin^2\theta_0 + \epsilon^2\cos^2\theta_0} = R\sqrt{1+(\epsilon^2-1)\,|\mathbf{q}\cdot\mathbf{n}|^2/q^2}$. Here $\mathbf{n}$ is the unit vector oriented along the particle axis and θ_0 the angle between $\mathbf{n}$ and the transferred momentum $\mathbf{q}$. In contrast with the forward depolarized scattering in the Rayleigh regime, here the relative amplitude of the fluctuation in the scattered intensity due to a rotation of the particle does not depend at all on the optical contrast, while is strongly influenced by the overall particle size and by the collection angle, which in turn determines the transferred momentum q.

This property, namely the fact that fluctuation in the intensity of the light scattered at a large angle by an ensemble of anisotropic colloidal particles reflects also its rotational dynamics, has been exploited in DLS for accessing its roto-translational dynamics, as a complementary approach with respect to low angle depolarized scattering measurements [20, 31, 32]. Eq. 12 takes a particularly simple form if the particle is not too large compared to the inverse transferred momentum. In fact, for a relatively small uniaxial anisotropic particle (for which $qL \lesssim 1$, where L is its longer dimension), the expression in Eq. 11, can be expanded in (qL), leading to:

$$F \simeq 1 - \frac{q^2}{V}\left[I_{zz} + 2\left(I_{xx} - I_{zz}\right)\cos^2\theta_0\right] \tag{13}$$

or, to the same order in (qL), to

$$P = |F|^2 \simeq 1 - \frac{2q^2}{V}\left[I_{zz} + 2\left(I_{xx} - I_{zz}\right)\cos^2\theta_0\right], \tag{14}$$

where $I_{xx} = \int_V d^3\mathbf{x}\left(x^2+z^2\right)$ and $I_{zz} = 2\int_V d^3\mathbf{x}x^2$ are the diagonal elements of the particle tensor of inertia [7], and θ_0 is the angle between the axis of the particle and the transferred momentum $\boldsymbol{q}$. The simple harmonic dependence of the scattered intensity on θ_0 described by Eq. 14 will be used in the following paragraphs to link the correlations of the scattered intensity to the statistical properties of the rotational motion of the particle.

3.2. Dark field microscopy

Dark field imaging In the context of optical microscopy, the term dark field (DF) indicates a family of microscopy configurations characterized by the fact that optics and thus only the light scattered from the sample contributes to the image. In practice, this can be obtained in a number of different ways, for example by using dedicated illumination stages. A common implementation, which is compatible with most commercial inverted microscopes is the one reported in Fig. 1 a), where a schematic representation of a microscope with Koehler illumination is shown. In this configuration, a circular aperture (1) or radius R_{ring} carved into an opaque mask is placed in the back focal plane of the condenser lens (2), of focal length $(FL)_{cond}$. In this condition the object plane (3) is illuminated only by rays forming an angle $\theta \simeq \arcsin(NA)_c$, where $(NA)_c = \arctan\left[R_{ring}/\left(FL\right)_{cond}\right]$. The dark field condition is achieved by using an objective lens (4,5) with numerical aperture $(NA)_o < (NA)_c$, so that the transmitted beam is not collected by the objective. In practice, this is commonly achieved by coupling a high numerical aperture phase contrast ring with a low power objective. In this configuration, the illumination beam can be thought of as the incoherent superposition of many plane waves propagating at angles $\theta \simeq \arcsin\left(NA\right)_c$ with respect to optical axis *i.e.* the sample is illuminated by a collection of uncorrelated coherent patches of transverse size $\Lambda_s \simeq \lambda/(NA)_c$. Since $\left(NA\right)_o < \left(NA\right)_c$, the size of these coherent patches is smaller than the transverse size $\Lambda_o \simeq \lambda/\left(NA\right)_o$ of the objective PSF. For this reason, the imaging process is to all effects incoherent, as interference effects between different scattering centers are negligible. For this reason, we refer to this configuration as Incoherent Dark Field Microscopy (IDFM).

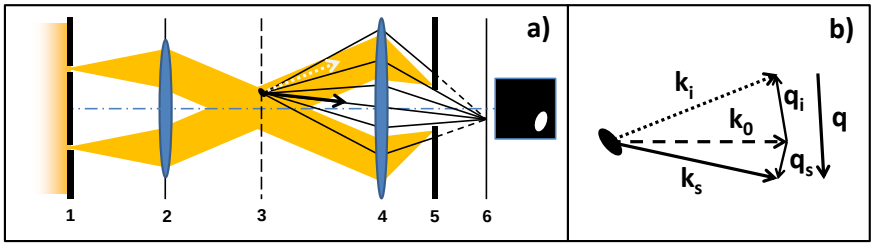

Figure 1. a) Schematic representation of an Incoherent Dark Field microscopy (IDFM) set-up with Koehler illumination: 1-beam stop, 2-condenser lens, 3-object plane, 4-objective lens, 5-objective exit pupil, 6-image plane. b) Elementary scattering process contributing to the image formation in IDFM. $\mathbf{k}_i$ denotes the incident wave-vector, $\mathbf{k}_s$ is the scattering wave-vector, $\mathbf{q} = \boldsymbol{k}_s - \boldsymbol{k}_i$ is the transferred momentum, and $\mathbf{k}_0$ the wave-vector oriented along the optical axis. The transferred momentum can be also written as $\boldsymbol{q} = \boldsymbol{q}_s - \boldsymbol{q}_i$, where $\boldsymbol{q}_s = \boldsymbol{k}_s - \boldsymbol{k}_0$ and $\boldsymbol{q}_i = \boldsymbol{k}_i - \boldsymbol{k}_0$.

According to the nomenclature introduced in [24], IDFM is thus a *linear* imaging system and can be thus profitably used for Digital Fourier Microscopy experiments, where a *linear* space-invariant imaging system turns out to beneficial [16]. We note that, as pointed out in Ref. [21], dark field imaging can in some cases lead to a non-homogeneous illumination pattern, which violates the space-invariant assumption. In our optical set-up this effect was negligible, in that the illumination was found to be uniform across the entire field of view.

Clearly, other implementations of dark field imaging, alternative to IDFM, exist, but not all of them are linear space-invariant and thus suitable for Digital Fourier Microscopy. An explicit example along this line is presented in Appendix B.

The incoherent dark field microscope as a fixed, non-zero angle scattering set-up In a dark field microscope the main contribution to the particle image intensity comes from light scattered at a non-zero angle, roughly corresponding to the illumination numerical aperture. As a consequence, if the particle is anisotropic, its reorientation produces a modulation in the image intensity. This property opens to the possibility of exploiting IDFM to study the rotational dynamics of anisotropic particles. The main elements of typical dark field microscopy setup are shown in the simplified scheme in Fig. 1. The elementary scattering process contributing to the image formation is shown in Fig. 1 b), where $\mathbf{k}_i$ denotes the incident wave-vector, $\mathbf{k}_s$ is the scattering wave-vector and $\mathbf{q} = \mathbf{k}_s - \mathbf{k}_i$ is the transferred momentum. By introducing $\mathbf{k}_0$ as the wave-vector oriented along the optical axis, having the same amplitude of $\mathbf{k}_i$ and $\mathbf{k}_s$ we can express the transferred wave-vector as $\mathbf{q} = \mathbf{q}_s - \mathbf{q}_i$, where $\mathbf{q}_s = \mathbf{k}_s - \mathbf{k}_0$ and $\mathbf{q}_i = \mathbf{k}_i - \mathbf{k}_0$. In the image plane, the total intensity I associated with the particle's image can be calculated as the (incoherent) sum of all such processes

$$I_p = V \int d\mathbf{q}_i \int d\mathbf{q}_s I_0(\mathbf{q}_0) P(\mathbf{q}_s - \mathbf{q}_i) T(\mathbf{q}_s) \tag{15}$$

where the function $I_0(\mathbf{q}_0)$, representative of the angular distribution of the illumination beam, weights the contribution of each incoming plane wave, the particle form factor $P(\mathbf{q})$ accounts for the scattering properties of the sample, and the incoherent transfer function $T(\mathbf{q}_s)$ quantifies the collection efficiency of the objective lens.

Our choice of a thin phase contrast ring of numerical aperture $(NA)_c$ makes the evaluation of the integral on the right hand side of Eq. 15 particularly simple, as $I_0(\mathbf{q}_0) \simeq I_0 \delta(|\mathbf{q}_0| - q^*)$,

where $q^* = 2k_0 \sin(\frac{\theta_c}{2}) \simeq k_0 \sin(\theta_c) = k_0 (NA)_c$. In general, $T(\mathbf{q})$ is an azimuthally symmetric function of width $\sim k_0 (NA)_o < k_0 (NA)_c$ centered around $\mathbf{q} = 0$. If we take the (rather crude) approximation: $T(\mathbf{q}_s) \simeq \delta(\mathbf{q}_s)$, corresponding to considering only the light scattered along the optical axis, we obtain the following simple result, where the total intensity of the particle's image is written as an azimuthal average of the particle form factor performed for $|\mathbf{q}| = q^*$: $I_p \propto \int d\mathbf{q}\delta(|\mathbf{q}| - q^*)P(\mathbf{q}) = \int_0^{2\pi} d\alpha P\left(\left[\begin{array}{ccc} q_\perp^* \cos\alpha, & q_\perp^*, \sin\alpha, & q_\parallel^* \end{array}\right]\right)$, where $q_\perp^* \simeq q^*$ and $q_\parallel^* \simeq 0$ are the projections of the transferred momentum in the direction perpendicular and parallel to the optical axis, respectively . In IDFM, the main contribution to the particle image intensity comes from light scattered at a non-zero angle, roughly corresponding to the illumination numerical aperture. If we assume for the form factor P the expression given in Eq. 14, I_p can be easily integrated leading to:

$$I_p \propto 1 - \frac{2q^{*2}}{V}\left[I_{xx} + (I_{zz} - I_{xx})\sin^2(\theta)\right] \tag{16}$$

or, equivalently

$$I_p = I_{p,0}\left[1 + cY_{20}(\theta)\right] \tag{17}$$

where $Y_{20}(\theta) = \sqrt{\frac{5}{16\pi}}\left(3\cos^2\theta - 1\right)$ is the spherical harmonic of order 2,0, θ is the angle between the axis of the particle and the optical axis, $I_{p,0}$ is a constant amplitude and c is a constant. Eq. 17 shows that the intensity signal due to an anisotropic particle depends on the particle orientation with respect to the optical axis, which explains why a particle that undergoes a rotational Brownian motion appears as a randomly blinking object. We note that considering a finite value for the objective numerical aperture does not affect this result. In fact, in that case I_p is still given by the integral of $P(q)$ over an annular region of radius q^* but with a finite width $\sim k_0 (NA)_o$, which does not affect the angular dependence of I_p in Eq. 17 but only the prefactor c. We note that Eq. 17 holds under the same hypotheses under which Eq. 14 is valid, namely that the $Lq^* \lesssim 1$, where L is longer dimension of the particle. For very large particles a more complex expression is expected, involving higher order spherical harmonics.

Dark field DDM probes the roto-translational dynamics of anisotropic particles The fact that the image intensity corresponding to one particle depends on the particle orientation can be in principle used to assess the rotational dynamics by studying the characteristic time of blinking in movies obtained by IDFM (see Supplementary Movie SM01 and SM02). For the case of interest in this work, *i.e.* when the particle undergoes a rotational Brownian motion, its rotational diffusion coefficient D_R can be obtained by calculating the intensity temporal auto-correlation function

$$C_p(\Delta t) = \langle I_p(t + \Delta t)I_p(t)\rangle = I_{p,0}^2\left(1 + c^2 e^{-6D_R t}\right), \tag{18}$$

whose characteristic time $(6D_R)^{-1}$ would give immediate access to the rotational diffusion coefficient D_R [7]. However, measuring $C_p(\Delta t)$ is usually quite difficult: for instance, particles can disappear from the image when they exit the focal region or two particles might superimpose along the optical axis and give rise to spurious effects. These difficulties can be bypassed by working in the wave-vector space, as done in Dark Field Differential Dynamic Microscopy (d-DDM)[21]. The image intensity distribution of a collection of identical particles observed in IDFM is given by

$$I_s(\mathbf{x}, t) = \sum_n I_p^{(n)}(t)\psi(\mathbf{x} - \mathbf{x}_n) \tag{19}$$

where $\psi(\mathbf{x})$ is a function that describes the distribution of the individual scatterers in real space. If $\hat{I}_s(\mathbf{q},t)$ is the spatial Fourier transform of $I_s(\mathbf{x},t)$, an alternative quantification of the particle dynamics is provided by the *intermediate scattering function*

$$\left\langle \hat{I}_s(q,t+\Delta t)\hat{I}_s^{\,*}(q,t)\right\rangle = N|\psi(q)|^2 C_p(\Delta t)e^{-D_T q^2 \Delta t} \tag{20}$$

where D_T is the translational diffusion coefficient of the particles. Eq. 20 can be rewritten by introducing the *normalized intermediate scattering function [7]*

$$f(\mathbf{q},\Delta t) = \frac{\left\langle \hat{I}_s(q,t+\Delta t)\hat{I}_s^{\,*}(q,t)\right\rangle}{\langle |I(q,t)|^2\rangle} = \alpha e^{-\Gamma_1(q)\Delta t} + (1-\alpha)e^{-\Gamma_2(q)\Delta t}, \tag{21}$$

where the contribution of the two relaxation modes with decay rates $\Gamma_1 = 6D_R + D_T q^2$ and $\Gamma_2 = D_T q^2$ can be appreciated. This form for the intermediate scattering function is pretty common, as is found also in depolarized DLS and p-DDM experiments [6, 13].

4. Results and discussion

In this Section, we demonstrate d-DDM as an effective powerful tool for the simultaneous determination of the translational and rotational dynamics by presenting results obtained with two representative samples: a suspension of quasi-index matched anisotropic colloidal particles (non-motile rod-shaped bacteria) and a suspension of quasi-monodisperse spherical colloids both in a non-aggregated state and forming small clusters.

4.1. Bacteria

A first set of measurements was performed on a suspension of density-matched non-motile coliform bacteria, prepared as described in the Material and Methods Section. Movies of the sample are acquired with dark field, bright field and phase contrast microscopy. A representative dark field image of the sample is shown in Fig. 2 (see also Supplementary Movie SM01): the bacterial particles appear as bright spots diffusing on a dark background and whose intensity fluctuates with a characteristic time of about 1 s. We will show that these two processes, namely, the concentration fluctuation due to the translational motion of the particles and the intensity fluctuations caused by the rotational dynamics of single particles, are well captured by the d-DDM analysis.

In Fig. 3 we show for some representative values of the wave-vector q, logarithmically spaced in the in range [0.075, 2.3] μm^{-1}, the intermediate scattering functions obtained with d-DDM analysis. As expected from Eq. 21, the observed relaxation exhibits two distinct decays. This is particularly evident in the low-q regime, where the time-scale separation between the two decays is more pronounced (see Fig. 3 b). The intermediate scattering functions are well described by a sum of two simple-exponential decays (continuous lines in Fig. 3). Fitting the obtained curves to Eq. 21 provides thus an estimate for the two q-dependent relaxation rates $\Gamma_1(q)$ and $\Gamma_2(q)$. The so-obtained Γ_1 and Γ_2 are shown in Fig. 4 together with the best fitting curves: $\Gamma_1(q) = D_T q^2 + 6D_R$, and $\Gamma_2(q) = D_T q^2$. From this last fit we obtain an estimate for the translational and the rotational diffusion coefficient of the bacteria: $D_T = (1.57 \pm 0.02)\cdot 10^{-1}$ $\mu m^2 s^{-1}$ and $D_R = (1.5 \pm 0.1)\cdot 10^{-1}$ s^{-1}.

The simultaneous measurement of both D_T and D_R allows estimating the size of the bacterial particles. We consider two simple models, for which analytical expressions for the diffusion coefficients are available, namely a spheroid of semi-axes a, b, and$c$, with $b = c$ [33] and a cylinder

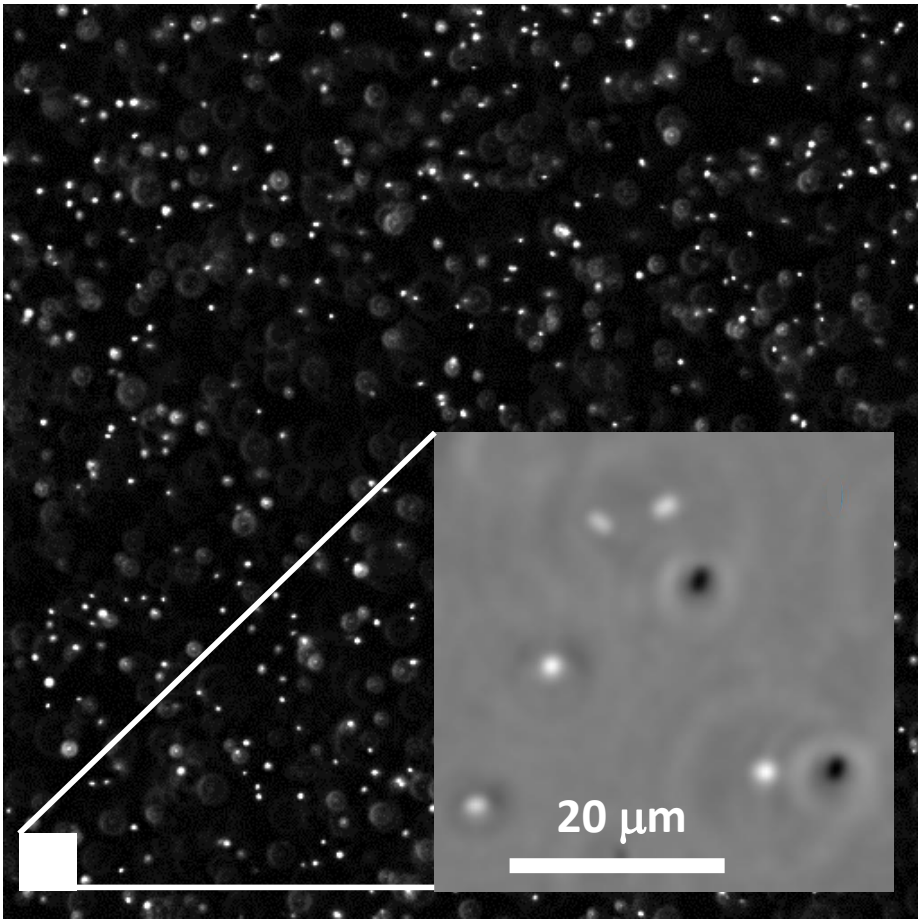

Figure 2. Main panel: representative dark field image of the bacterial suspension, where the optical background has been subtracted as described in the Material and Methods Section. Inset: representative phase-contrast image of the same sample.

of length L and radius r [34, 35]. Explicit expression for D_R and D_T in the two cases are reported in Appendix A and can be inverted numerically to determine the best estimates for the geometrical parameters in the two cases. In particular, it is convenient to parametrize the spheroid by expressing the length of the semi-axes $[a, b, c]$ in terms of the radius $\bar{R}$ of the sphere with equal volume and of the eccentricity parameter $\epsilon = \frac{a}{b}$, as $[a, b, c] = \bar{R}\epsilon^{-1/3}\,[\epsilon, 1, 1]$. We obtain: $\bar{R} = 0.70 \pm 0.02\ \mu m$, $\epsilon = 2.3 \pm 0.3$ for the spheroid and $L = 1.6 \pm 0.2\ \mu m$, $r = 0.6 \pm 0.2\ \mu m$ for the cylinder. We note that both models provide meaningful results, that are in good mutual agreement and are fully compatible with both literature values [36, 37] and direct, high magnification microscopy observations (see Fig. 2).

As a consistency check, we also analyzed bright field and phase-contrast movies of the same sample. In both cases, the obtained intermediate scattering functions show a single decay that is very well fitted by a simple exponential function (data not shown). The corresponding q-dependent

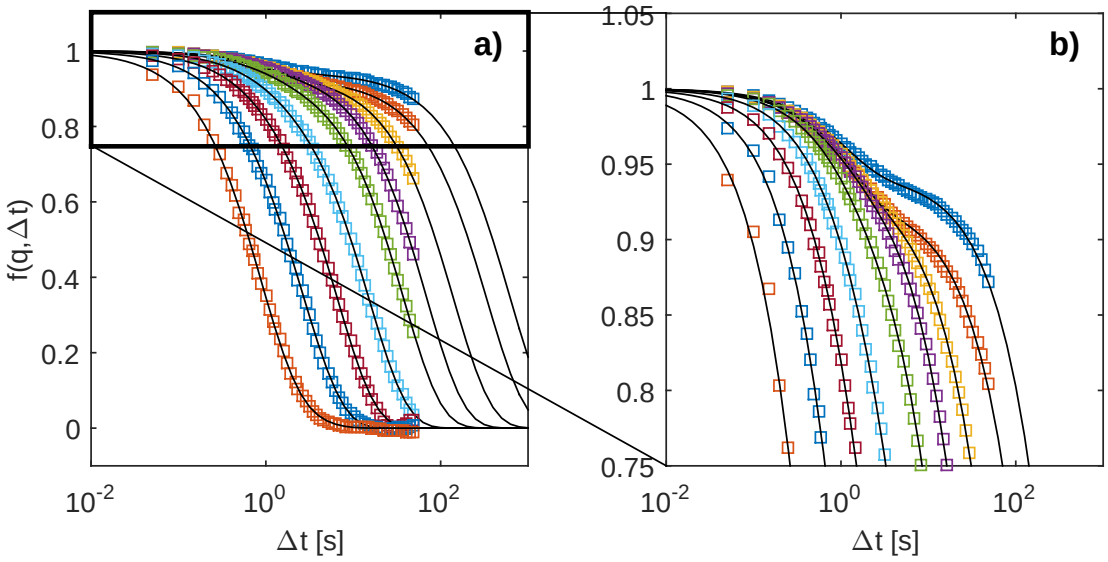

Figure 3. Symbols: intermediate scattering function $f(q, \Delta t)$ obtained for different wave vectors q = 0.075, 0.11,0.19, 0.30, 0.44, 0.65, 0.98, 1.5, 2.3 μm^{-1} in d-DDM experiments. Continuous lines: best fitting curves with the model function given in Eq. 21.

relaxation rates are reported in Fig. 4 and exhibit a very clean q^2 scaling and the estimated translational diffusion coefficient $D_T = (1.58 \pm 0.01)\ \mu m^2/s$ is in excellent agreement with the results of d-DDM. Of note, the wave-vector range over which a reliable estimate of the dynamics can be obtained is not the same for all the imaging conditions. In particular, we observe that, although dark field and bright field measurements are performed with the same objective, frame rate and duration of the acquisition, dark field DDM is much more effective in probing the dynamics in the low-q regime. This can explained by inspecting the static scattering amplitudes $A(q)$ obtained from the DDM analysis in the two datasets show in the inset of Fig. 4, which outlines the effect of the different transfer functions of the two methods. The bright field amplitude shows the characteristic depression at low q, reflecting the fact that bacteria, being quasi-index matched with the solvent, behave as phase objects [24]. On the contrary, the dark field amplitude is a monotonically decreasing function of q. The phase contrast data, being obtained with a different microscope objective, with larger magnification and numerical aperture (40 vs 10 and 0.6 vs 0.15), cover a q range shifted by approximately half a decade to larger wave-vectors.

4.2. Spherical colloids

A second set of d-DDM measurements was performed on a suspension of monodisperse spherical latex particles. A first sample (Sample 1) was prepared with a 5 minutes sonication stage before the measurement, as described in the Materials and Methods Section. Surprisingly, we found that d-DDM analysis showed two distinct decays $\Gamma_1(q)$ and $\Gamma_2(q)$ for the ISF (5), as previously found for the bacteria. This finding contrasted our expectation to observe a single relaxation mode due to translational diffusion of the particles. In order to better understand the reason of such unexpected

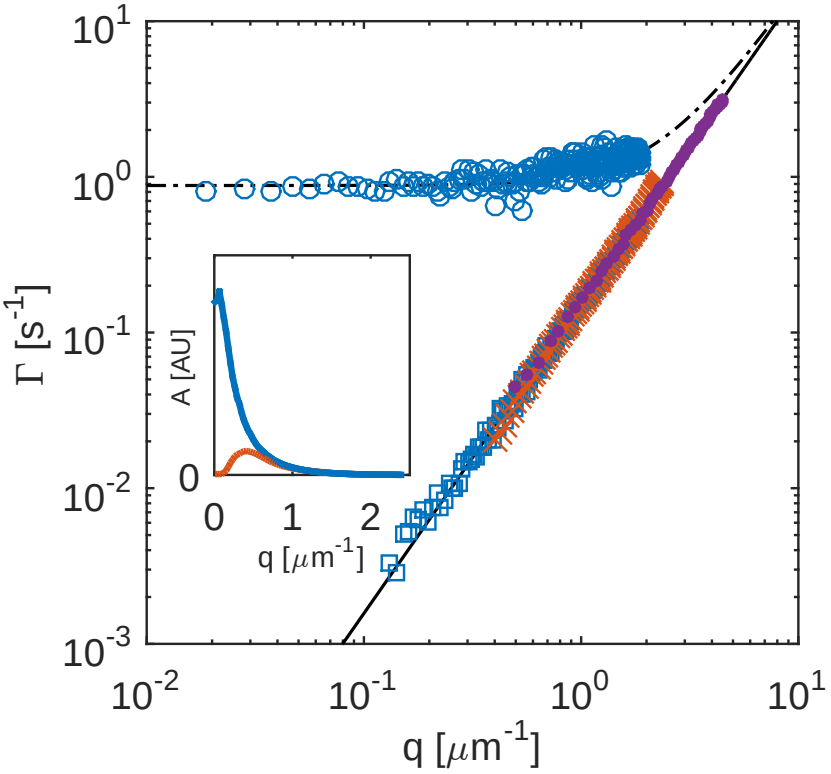

Figure 4. Decorrelation rates as a function of the wave-vector q obtained from the fit of the intermediate scattering functions obtained in dark field (open blue circles and squares), in bright field (orange crosses) and in phase-contrast (purple circles) microscopy experiments on a dilute bacterial dispersion. The dash-dotted and the continuous lines are the best fits to the curves $\Gamma_1(q) = 6D_R + D_T q^2$ and $\Gamma_2(q) = D_T q^2$, respectively, which lead to the estimates $D_T = (1.57 \pm 0.02) \cdot 10^{-1}$ $\mu m^2 s^{-1}$ and $D_R = (1.5 \pm 0.1) \cdot 10^{-1}$ s^{-1}. Bright field and phase-contrast data provided the value $D_T = (1.58 \pm 0.01)$ $\mu m^2/s$, obtained by fitting the experimental data to the curve $\Gamma_2(q) = D_T q^2$ (fitting curve not shown). Inset: static amplitude $A(q)$ obtained with the same microscope objective from DDM analysis of bright field (red squares) and dark field (blue circles) movies of the same bacterial dispersion. While the dark field amplitude is a decreasing function q, the optical transfer function for the bright field experiments is characterized by a visible depression at small scattering wave-vectors.

behavior we thus performed a bright field DDM experiment on the same sample: as expected for a reasonably monodisperse sample, the experimental ISFs were well fitted to a single exponential decay and the so-obtained relaxation rate $\Gamma(q)$ was well fitted to the function $\Gamma(q) = D_T q^2$ (Fig. 5). The estimate $D_T^{BF} = 0.475 \pm 0.05$ µm^2/s for the translational diffusion coefficient of the particles is fully compatible with the value found in dark field experiments, which gave $D_T^{DF} = 0.49 \pm 0.01$ µm^2/s and $D_R = 1.3 \pm 0.05$ s^{-1} for the translational and rotational diffusion coefficients, respectively. However, none of them was found to be compatible with the value $R_H^{cert} = 0.37 \pm 0.2$ μm, certified by the producer for the hydrodynamic radius of the particles. Both values $R_H^{BF} = 50.3 \pm 0.05$ μm

and $R_H^{DF} = 49 \pm 1\ \mu m$, obtained from D_T^{BF} and D_T^{DF}, respectively, *via* the Stokes-Einstein relation are about 30% larger than the nominal value. We interpreted all these results as consequences of the presence of anisotropic particles in suspension, originated from aggregation of the spherical particles. Careful inspection of dark field movies (Supplementary Movie SM02) further supported this hypothesis in that it pointed to the presence of a small number of blinking particles.

To obtain final confirmation, we performed measurements on a second sample (Sample 2) that was carefully prepared from the same batch of particles by using a longer sonication stage (30 minutes instead of 5). With Sample 2, the results of DDM analysis of bright field and dark field movies (see Supplementary Movie SM03) confirm the absence of aggregates. In both cases, the ISFs exhibit a *single* exponential decay, with a relaxation rate displaying a clean quadratic scaling with q, from which we obtain the estimate $D_T = 0.695 \pm 0.01$ µm^2/s for the translational diffusion coefficient (Fig. 5). The extracted hydrodynamic radius $R_H = 35 \pm 1\ \mu m$ is now fully compatible with the nominal size of the particle, as certified by the producer. We could therefore safely conclude that Sample 1 contained aggregated particles and that d-DDM provides a very powerful means to spot the presence of small aggregates in colloidal dispersions of spherical particles. In particular, when sizing unknown samples, it would be recommended to complement bright field DDM experiments with dark field ones, to check whether a rotational diffusion decay mode due to aggregates is present or not.

We then turned to assessing how far can d-DDM be brought in obtaining information on the aggregates. To this aim we evaluated the values expected for the translational and rotational diffusion coefficients of small clusters of particles (dimers, trimers, tetramers, etc.) [38]. In particular, the value ${D^{cert}}_T = 0.65$ µm^2/s, corresponding to the hydrodynamic radius certified by the producer, gives the following values for small clusters: $D_T^{di} = 0.48$ µm^2/s (dimers), $D_T^{tri} = 0.41$ µm^2/s (trimers), and $D_T^{tetra} = 0.38$ µm^2/s (tetramers). We note that these values are very close to each other, which explains why translational diffusion does not discriminate very effectively between these contributions. This is confirmed by our d-DDM results, as we found that the translational diffusion coefficient extracted with d-DDM exhibited an intermediate value between the expectation for monomers and for the small clusters. By contrast, the rotational diffusion coefficient is not sensitive to the presence of monomers. Consistently, the value obtained with d-DDM ($D_R = 1.3 \pm 0.05\ s^{-1}$) was found to be within the range of the rotational diffusion coefficient expected for small clusters: $D_R^{di} = 1.39\ s^{-1}$ (dimers), $D_T^{tri} = 0.87\ s^{-1}$ (trimers), and $D_R^{tetra} = 0.67\ s^{-1}$ (tetramers).

In order to check the consistency of this picture, we performed a detailed Video Particle Tracking (VPT) analysis on the same movies, which is very delicate and time consuming but provides a more detailed information about the sub-populations of which the sample is composed. Particles trajectories are obtained with the Particle Tracker Plugin, included in the Mosaic Suite for ImageJ. With a custom software written in Matlab, we extracted from each trajectory the particles mean squared displacement and, by fitting the resulting curve as a function of the time delay we obtain and estimate for the translational diffusion coefficient D_T of each single particle. By rejecting trajectories shorter than 200 time steps, we obtained D_T for about 1000 particles for each sample. In Fig. 6, we report the histograms representing the distributions of the values of D_T obtained for each of the two samples. For Sample 2, the distribution of D_T is fairly symmetric and it is well described by a Gaussian function with mean value $\bar{D}_T = 0.69\ \mu m^2/s$ and standard deviation $\sigma_{D_T} = 0.1\ \mu m^2/s$. This result is compatible with a moderately dispersed distribution peaked around a value that is in excellent agreement with estimated $D_T = 0.695 \pm 0.01$ µm^2/s obtained for the translational diffusion coefficient from the d-DDM analysis. For Sample 1, the same SPT-based

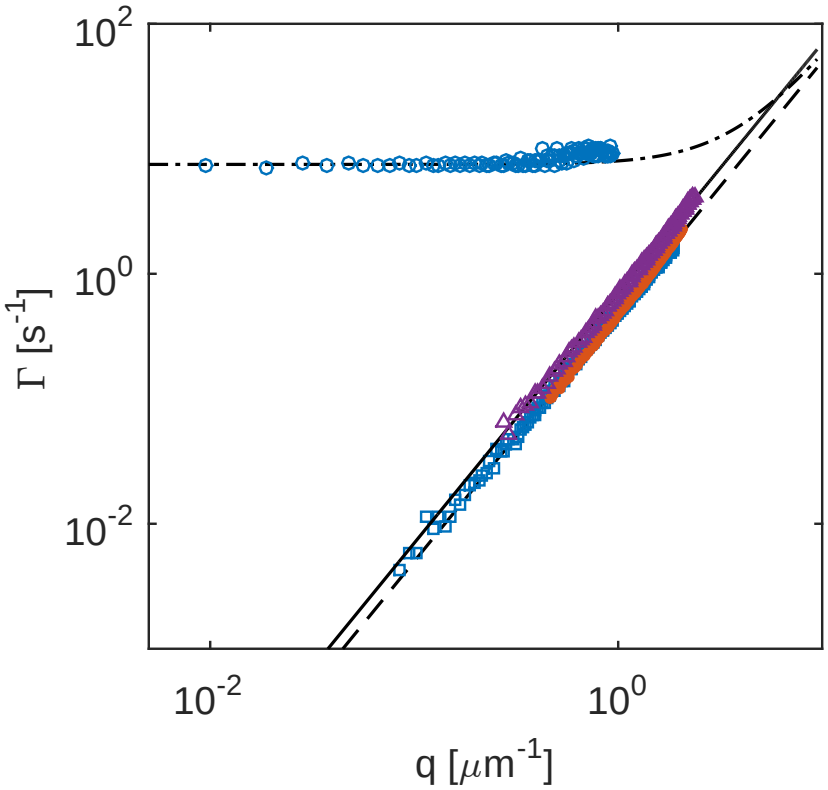

Figure 5. Decorrelation rates obtained from the fit of the intermediate scattering functions obtained in dark field (open blue circles and squares) and in bright field (orange dots) microscopy experiments on a partially aggregated suspension of spherical colloidal particles (Sample 1). The dash-dotted and the dashed lines are the best fits to the curves $\Gamma_1(q) = 6D_R + D_T^{BF}q^2$ and $\Gamma_2(q) = D_T^{BF}q^2$, respectively, which lead to the estimates $D_T^{DF} = 0.49 \pm 0.02\ \mu m^2 s^{-1}$ and $D_R = 1.3 \pm 0.05\ s^{-1}$. Bright field data provided the value $D_T^{BF} = 0.475 \pm 0.05\ \mu m^2 s^{-1}$, obtained by fitting the experimental data to the curve $\Gamma_2(q) = D_T^{BF}q^2$ (fitting curve not shown). Upward purple triangles correspond to the single decorrelation rate $\Gamma(q)$ measured in a dark field microscopy experiment on a non-aggregated suspension of the same particles (Sample 2), The continous line is the best fit to the curve $\Gamma(q) = D_T q^2$, leading to the estimate $D_T = 0.695 \pm 0.01$ $\mu m^2 s^{-1}$.

analysis provides a completely different result. The distribution of D_T is broader and, beside a peak centered about a value compatible with $\bar{D}_T$, a secondary peak for $D_T \simeq 0.4\ \mu m^2/s$ is also clearly visible. As shown in Fig. 6, the range covered by this secondary peak is compatible with the translational diffusion coefficients expected for small clusters of monomers, assuming $\bar{D}_T$ as the diffusion coefficient of a monomer. These results strongly corroborate our interpretation and confirm that d-DDM can be used to measure with high sensitivity the translational dynamics of spherical colloids and to spot aggregation of spherical particles in a simple and effective way.

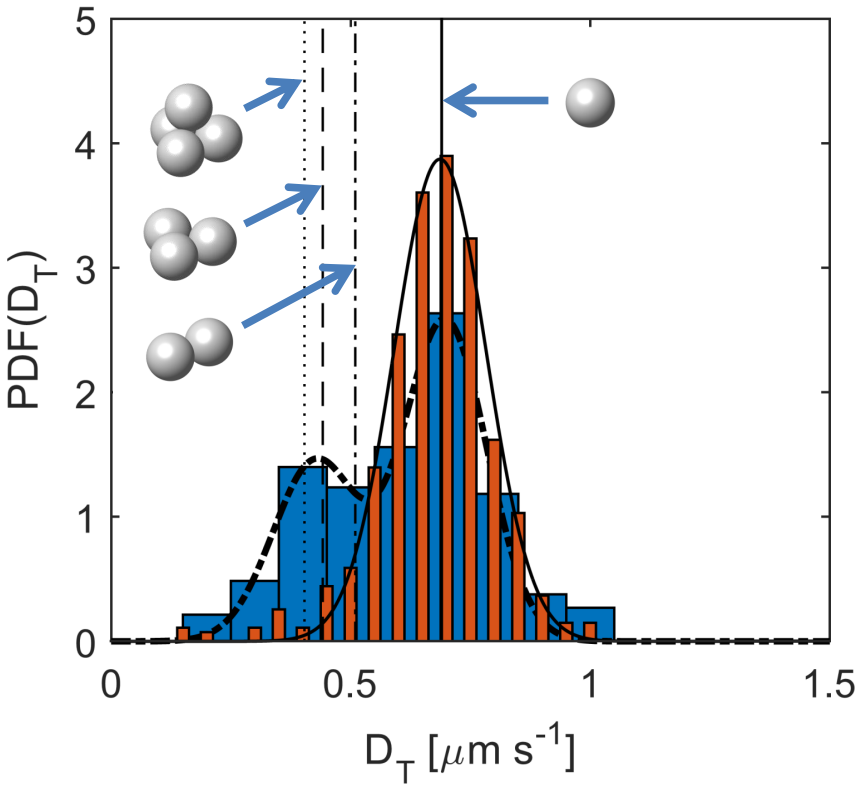

Figure 6. Histograms of the distribution of translational diffusion coefficient for Sample 1 (large blue bars) and for Sample 2 (thin orange bars) as determined from VPT. The continous vertical line correspond to $\bar{D}_T = 0.69\ \mu m^2 s^{-1}$, obtained by fitting the histogram obtained from Sample 2 to a Gaussian function (continous curve). The histogram for Sample 1 is well described as the sum of two Gaussian functions (heavy dashed-dotted curve) centered in $D_T \simeq 0.7\ \mu m^2 s^{-1}$ and $D_T \simeq 0.4\ \mu m^2 s^{-1}$, respectively. This second value falls within the range of the translational diffusion coefficients expected for small clusters of monomers, assuming $\bar{D}_T$ as the diffusion coefficient of a monomer. The vertical dashed-dotted, dashed and dotted lines correspond to the expected values for dimers, trimers and tetramers, respectively.

5. Conclusions

In this work, we have shown that the recently introduced Dark Field Differential Dynamic Microscopy [21] is a simple and powerful tool for the simultaneous determination of the roto-translational dynamics of anisotropic microparticles in suspension. Our experiments with bacterial suspensions showed that d-DDM is somehow complementary to the recently proposed polarized-DDM [13], in that the latter may fail with particles characterized by moderate shape anisotropy and good refractive index-matching with the dispersion medium.

We also showed that the peculiar nature of the dark field signal associated with the rotational dynamics, makes d-DDM very effective in spotting and quantifying the presence of anisotropic aggregates of isotropic particles, even though whenever the particles are large enough, particle

tracking may provide a better tool for a detailed analysis of aggregated samples in which clusters are present. On the other hand, d-DDM analysis is statistically more robust and does not require the intervention of an experienced user for the fine tuning of the parameters involved in the image processing procedure.

These promising results open to the possibility of studying with d-DDM more complex and challenging systems. For example, it is know that, for motile bacteria, the rotational dynamics is very different from the purely Brownian one [39] and that a non-trivial interplay exists between rotational and transational degrees of freedom [40]. d-DDM could allow the simple, high-throughput, characterization of this complex dynamics, possibly combination with other quantitative microscopy methods, like for example standard phase contrast DDM [41] or the so-called dark field flicker microscopy [42], that has been used for monitoring the rapid periodic fluctuation associated with the beating of flagella.

Another field of potential application is the optical characterization of the mechanical properties of soft materials, the realm of microrheology [43, 44]. Passive microrheology, in particular, exploits the thermally excited positional fluctuations of immersed tracer particles to probe the viscoelastic moduli of the hosting fluid [45]. Very recently, DDM has been demonstrated to be a reliable route to microrheology, enabling the accurate, tracking-free determination of the mean squared displacement of probe particles in a variety of imaging conditions [46, 47]. In view of the results presented in this work, we expect that d-DDM, in combination with calibrated anisotropic tracers, could provide the ideal ground to extend these ideas also to the rotational degree of freedom, enabling the simultaneous execution of translational and rotational microrheology experiments [48, 49]. While this combination could appear redundant in the case of a perfectly homogeneous fluid - where the two approaches are expected to give equivalent results - it could quite valuable in the presence of sources of non-ideality in the system (*e.g.* inhomogeneity of the matrix or specific tracer-fluid interactions altering the boundary conditions at the surface of the particles). Since these effects, that can seriously compromise the reliability microrheology results, are expected to have a different impact on rotational and translational degrees of freedom, the execution of a combined experiment could allow to spot them effectively.

Moreover, since d-DDM is very sensitive in detecting the presence of anisotropic particles, it can be exploited as a quality control step during the preparation or the execution of experiments involving allegedly spherical colloidal particles or for real-time monitoring of aggregation processes and self-assembly. Another intersting application of the method could be in the on-line moniting of water quality [50]. In this case, the ability of d-DDM to spot the presence of particles in solution and, by providing an estimate of their dimensions and optical contrast, to discriminate between them, could make it an useful screening tool for the automatic identification of particularly important classes of contaminants, *in primis* bacteria.

Acknowledgments

We thank Silvia Biffi, Filippo Saglimbeni and Giovanni Tagliabue for help in the preparation of the samples and for early contributions to the project. We also thank Roberto di Leonardo and Claudio Maggi for insightful comments and discussions. RC, DP and FG acknowledge funding by the Italian Ministry of Education and Research, Futuro in Ricerca Project ANISOFT (RBFR125H0M) and by Fondazione CARIPLO-Regione Lombardia Project Light for Life (2016-0998). MB acknowledges funding from the European Union's Seventh Framework Programme (FP7) for Research, Technological Development and Demonstration through the NAPES project

(grant agreement no. 604241).

Appendix A. Roto-translational diffusion of spheroids and cylinders

In this Appendix we report analytic expressions available in the literature for the rotational and translational diffusion coefficient for a spheroidal particle [33] and for a cylinder [34, 35].

Spheroid The rotational and translational diffusion coefficients are given by, respectively

$$D_R = \frac{3k_BT}{32\pi\eta}\frac{\left(2a^2-b^2\right)S-2a}{a^4-b^4},$$

$$D_T = \frac{k_BT}{12\pi\eta}S.$$

Here $S = (2/k)\ln\left(\frac{a+k}{b}\right)$, $k^2 = a^2 - b^2$, k_B is the Boltzmann constant, T is the absolute temperature and η is the solvent viscosity. The spheroid is assumed to be prolate with semi-axes $[a, b, c]$, with $a > b = c$.

Cylinder The rotational and translational diffusion coefficients are given by, respectively

$$D_R = \frac{3D_0}{\pi L^2}\left(\ln p - 0.662 + 0.917/p - 0.050/p^2\right),$$

$$D_T = \left(D^{\parallel} + 2D^{\perp}\right)/3,$$

where $D^{\perp}$and $D^{\parallel}$ are the translational diffusion coefficients along the direction perpendicular and parallel to the axis of the particle, respectively:

$$D^{\perp} = \frac{D_0}{4\pi}\left(\ln p + 0.839 + 0.185/p + 0.233/p^2\right),$$

$$D^{\parallel} = \frac{D_0}{2\pi}\left(\ln p - 0.207 + 0.980/p - 0.133/p^2\right).$$

In the above expression $D_0 = k_BT/\eta L$, $p = L/\sigma$. σ and L are, respectively, the diameter and the length of the cylinder. All other quantities are defined as in case of the spheroid.

Appendix B. Coherent Dark Field Microscopy

In this Appendix we briefly discuss a dark field imaging system alternative to the Incoherent Dark Field Microscopy (IDFM) scheme discussed in the main text. The optical arrangement is schematically shown in Fig. B1 a), and it very similar to the one adopted in homodyne imaging and/or near-field scattering set-ups [15, 51].

The sample (3) is illuminated by a highly coherent beam (obtained for example by placing a pin hole (1) in the front focal plane of the condenser lens (2)) and the transmitted light is blocked by a small opaque patch placed in the back focal plane (5) of the objective lens (4). We call this configuration Coherent Dark Field Microscopy (CDFM), since the sample is ideally illuminated by a single plane wave propagating along the optical axis and the light scattered by different points of the sample always bears a well defined relative phase. The superposition of the scattering patterns

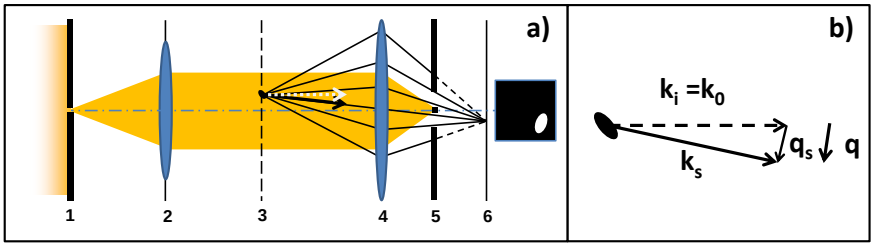

Figure B1. a) Schematic representation of a Coherent Dark Field Microscopy (CDFM) set-up, similar to custom bench-top homodyne near-field scattering apparatus. 1-pin hole, 2-condenser lens, 3-object plane, 4-objective lens, 5-objective exit pupil a with beam stop in the focal point, 6-image plane. (see text for additional details). d) Scattering process in CDFM. The incident wave-vector $\mathbf{k}_i$ is parallel to optical axis. The transferred momentum $\boldsymbol{q}$ is given by $\boldsymbol{k}_s - \boldsymbol{k}_i$, where $\boldsymbol{k}_s$ is the scattering wave vector.

from different points of the sample takes thus place on a coherent basis, since interference effects cannot be neglected. In other terms, the image formation process is linear in the complex amplitude rather than in the intensity, as it is for IDFM [52]. As a consequence, IDFM is a linear imaging system, while CDFM is not, in that the image intensity recorded in presence of two particles is not given by just the sum of the intensities associated with the two particles imaged separately. For this reason, IDFM is to be preferred for Digital Fourier Microscopy experiments, where a linear space-invariant imaging system turns out to beneficial [16].

References

[1] Haw M D 2002 *J. Phys.: Condens. Matter* **14** 7769

[2] Bian X, Kim C and Karniadakis G E 2016 *Soft Matter* **12** 6331–6346

[3] Coffey W T and Kalmykov Y C 2017 *The Langevin Equation With Applications to Stochastic Problems in Physics, Chemistry and Electrical Engineering* 2nd ed (World Scientific)

[4] Doi M 2011 *J. Phys.: Condens. Matter* **23** 284118

[5] Doi M 2013 *Soft Matter Physics* (Oxford University Press)

[6] Piazza R, Degiorgio V, Corti M and Stavans J 1990 *Phys. Rev. B* **42** 4885

[7] Berne B J and Pecora R 2000 *Dynamic light scattering: with applications to chemistry, biology, and physics* (Dover Publications)

[8] Borsali R and Pecora R 2008 *Soft Matter Characterization* (Springer)

[9] Tsyboulski D A, Bachilo S M, Kolomeisky A B and Weisman R B 2008 *ACS Nano* **2** 1770–1776

[10] Eimer W, Williamson J R, Boxer S G and Pcora R 1990 *Biochemistry* **29** 799–811

[11] Lehner D, Lindner H and Glatter O 2000 *Langmuir* **16 (4)** 1689–1695

[12] Balog S, Rodriguez-Lorenzo L, Monnier C A, Michen B, Obiols-Rabasa M, Casal-Duja L, Rothen-Rutishauser B, Petri-Fink A, and Schurtenberger P 2014 *J. Chem. Phys.* **118** 17968

[13] Giavazzi F, Haro-Pérez C and Cerbino R 2016 *J. Phys.: Condens. Matter* **28** 195201

[14] Cerbino R and Trappe V 2008 *Phys. Rev. Lett.* **100** 188102

[15] Cerbino R and Vailati A 2009 *Curr. Opin. Colloid Interface Sci.* **14** 416–425

[16] Giavazzi F and Cerbino R 2014 *J. Opt.* **16** 083001

[17] Cerbino R and Cicuta P 2017 *J. Chem. Phys.* **147** 110901

[18] Glotzer S and Solomon M J 2007 *Nat. Mater.* **6** 557–562

[19] Kotlarchyk M, Chen S H and Asano S 1979 *Appl. Optics* **18** 2470–2479

[20] Pecora R 1968 *J. Chem. Phys.* **48** 4126–4128

[21] Bayles A V, Squires T M and Helgeson M E 2016 *Soft Matter* **12** 2440–2452

[22] Croccolo F, Brogioli D, Vailati A, Giglio M and Cannell D S 2006 *Appl. Optics* **45** 2166–2173

[23] Giavazzi F, Crotti S, Speciale A, Serra F, Zanchetta G, Trappe V, Buscaglia M, Bellini T and Cerbino R 2014 *Soft matter* **10** 3938–3949

[24] Giavazzi F, Brogioli D, Trappe V, Bellini T and Cerbino R 2009 *Phys. Rev. E* **80** 031403

[25] Wilson L G, Martinez V A, Schwarz-Linek J, Tailleur J, Bryant G, Pusey P and Poon W C 2011 *Phys. Rev. Lett.* **106** 018101

[26] Ferri F, D'Angelo A, Lee M, Lotti A, Pigazzini M C, Singh K and Cerbino R 2011 *Eur. Phys. J. Special Topics* **199** 139–148

[27] He K, Spannuth M, Conrad J C and Krishnamoorti R 2012 *Soft Matter* **8** 11933–11938

[28] Germain D, Leocmach M and Gibaud T 2016 *Am. J. Phys.* **84** 202–210

[29] Safari M S, Vorontsova M A, Poling-Skutvik R, Vekilov P G and Conrad J C 2015 *Phys. Rev. E* **92** 042712

[30] Van De Hulst H 1957 *Light scattering by small particles* (Wiley)

[31] King T A, Knox A and McAdam J D G 1973 *Biopolymers* **12** 1917–1926

[32] Schillen K, Brown W and Johnsen R M 1994 *Macromolecules* **27** 4825–4832

[33] Koenig S H 1975 *Biopolymers* **14** 2421–2423

[34] Tirado M M, Martínez C L and de la Torre J G 1984 *J. Chem. Phys.* **81** 2047–2052

[35] Lowen H 1994 *Phys. Rev. E* **50** 1232–1242

[36] Grossman N, Ron E and Woldringh C 1982 *J. Bacteriol.* **152** 35–41

[37] Nelson D and Young K 2000 *J. Bacteriol.* **182** 1714–21

[38] Hoffmann M, Wagner C S, Harnau L and Wittemann A 2009 *ACS Nano* **3** 3326–3334

[39] Saragosti J, Silberzan P and Buguin A 2012 *PLOS ONE* **7** e35412

[40] Patteson A E, Gopinath A, Goulian M and Arratia P E 2015 *Sci Rep.* **5** 15761

[41] Martinez V A, Besseling R, Croze O A, Tailleur J, Reufer M, Schwarz-Linek J, Wilson L G, Bees M A and Poon W C K 2012 *Biophys. J.* **103** 1637–1647

[42] Martinez V A, Schwarz-Linek J, Reufer M, Wilson L G, Morozov A N and Poon W C K 2014 *Proc. Natl. Acad. Sci. USA* **111** 17771–17776

[43] Cicuta P and Donald A M 2007 *Soft Matter* **3** 1449–1455

[44] Waigh T A 2016 *Rep Prog Phys* **79** 074601

[45] Mason T G and Weitz D A 1995 *Phys. Rev. Lett.* **74** 1250–1253

[46] Bayles A V, Squires T M and Helgeson M E 2017 *Rheologica Acta* **56** 863–869

[47] Edera P, Bergamini D, Trappe V, Giavazzi F and Cerbino R 2017 *arXiv preprint arXiv:1708.07170*

[48] Cheng Z and Mason T G 2003 *Phys. Rev. Lett.* **90** 018304

[49] Andablo-Reyes E, Díaz-Leyva P and Arauz-Lara J L 2005 *Phys. Rev. Lett.* **94** 106001

[50] Hojris B, Christensen S C B, Albrechtsen H J, Smith C and Dahlqvist M 2016 *Sci Rep.* **6** 23935

[51] Giglio M, Carpineti M and Vailati A 2000 *Phys. Rev. Lett.* **85** 1416–1419

[52] Goodman J 1996 *Introduction to Fourier Optics* 2nd ed (MaGraw-Hill)